A Transmitter–Receiver System for Long-Range Capacitive Sensing Applications

Peter Lindahl, *Member, IEEE*, Al-Thaddeus Avestruz, *Member, IEEE*, William Thompson,
Elizabeth George, Brian R. Sennett, and Steven B. Leeb, *Fellow, IEEE*

***Abstract*— Human occupancy detection and localization are important in a variety of smart building applications including building security, assisted living monitors, and energy-efficient heating ventilation and air cooling and lighting. Current implementation of such systems is limited by motion–sensor technologies, e.g., passive infrared (PIR) and ultrasonic sensors, which substitute as occupancy detectors but ultimately suffer from an inability to detect stationary objects. Capacitive sensing can detect stationary objects, but the technology has almost exclusively been developed for short-range human detection and localization, e.g., touch-screen human interfacing of smart devices. This paper presents a transmitter–receiver platform for research and development of capacitive sensing for long-range human occupancy detection and localization. During testing, the system revealed a detection range of 3.5 m, a typical room dimension in homes. Further, tests of a multitransmitter single-receiver system in a 3.2 m × 3.2 m space showed the system's potential for occupant localization. Ultimately, this system represents an alternative to PIR and ultrasonic motion sensors, and has the potential to increase smart building system implementation.**

***Index Terms*— Capacitance measurement, electrical capacitance tomography, hyper spectral sensors, identification of persons, motion detection.**

I. INTRODUCTION

CAPACITIVE sensing systems are ubiquitous in both design and application [1], [2]. Numerous consumer electronic systems, e.g., mobile phones, tablets, and computers, utilize capacitive sensing techniques for touch-sensitive human interfacing [3], [4], and research continues toward extending capacitive sensing utility for gesture sensing technology [5], [6].

Capacitive sensors are also used to detect human presence as part of larger systems. In the automotive industry, capacitive sensing has been widely researched as a method for seat occupancy detection [7]–[10], an important input for automated airbag deployment decisions. Other safety-related capacitive systems include capacitive networks for proximity sensing around chainsaw blades [11] and interdigital sensors for detecting human personnel in close proximity to robotic arms at production sites [12].

Despite their ubiquity, the majority of these applications feature short-range sensing on the order of centimeters or less. For example, the chainsaw protection system [11] has a range of approximately 15 cm and the gesture sensing technology [5] a range of 10 cm. In large part, the focus on short-range sensing applications is likely due to long-range sensing being inherently more difficult. Capacitive measurements made over long distances suffer from increased environmental noise, smaller signal levels, and nonlinearities caused by fringing electric fields.

Still, in recent years, some capacitive sensing systems with longer ranges have been developed for human detection. Pottier and Rasolofondraibe [13] designed a capacitive sensing system for a vehicle that can detect the presence of a human pedestrian at a distance of 1 m. Buller and Wilson [14] described a capacitive sensing system with a similar range for occupancy detection based on mutual capacitance measurements between a human occupant and the electrical wiring in a building.

Cooley *et al.* [15] and Avestruz *et al.* [16] also focused on utilizing electrical systems inherent in buildings for performing occupancy detection via capacitive sensing. In these studies, they modified fluorescent and LED lighting ballasts using their inherent high-frequency electrical switching to provide a source electric field. Differential receiver electrodes attached below the lamps collected the fringing fields from the ballast. As an occupant neared the lamp, some of the fringing fields shunted through the occupant to ground, thus affecting the capacitive coupling of the source and receive electrodes. These lamp-based systems achieved detection ranges of around 3 m [15].

This paper describes a novel long-range capacitive sensing system, which unlike those of [15] and [16] features standalone source and receive electrodes, thus eliminating the reliance on lights [17], [18]. This system is intended to be a platform for investigating capacitive sensing as an alternative to passive infrared (PIR) and ultrasonic sensors, which suffer as occupancy detectors due to high rates of false detections and an inability to detect stationary objects [19], [20]. Accurate occupancy detection and localization is important for a variety of applications including smart building heating ventilation and air cooling (HVAC) and lighting, automated assisted living monitoring, and building security.

Manuscript received January 16, 2016; revised April 6, 2016; accepted May 10, 2016. This work was supported in part by the Massachusetts Institute of Technology and Masdar Institute Cooperative Program and in part by The Grainger Foundation. The Associate Editor coordinating the review process was Dr. Jesús Ureña.

P. Lindahl and S. B. Leeb are with the Massachusetts Institute of Technology, Cambridge, MA 02139 USA (e-mail: lindahl@mit.edub).

A.-T. Avestruz is with the Department of Electrical and Computer Engineering, University of Michigan, Ann Arbor, MI 48109 USA.

W. Thompson is with Apple Inc., Cupertino, CA 95014 USA.

E. George is with Silicon Labs, Austin, TX 78701 USA.

B. R. Sennett is with Bose Corporation, Framingham, MA 01701 USA.

Color versions of one or more of the figures in this paper are available online at http://ieeexplore.ieee.org.

Digital Object Identifier 10.1109/TIM.2016.2575338

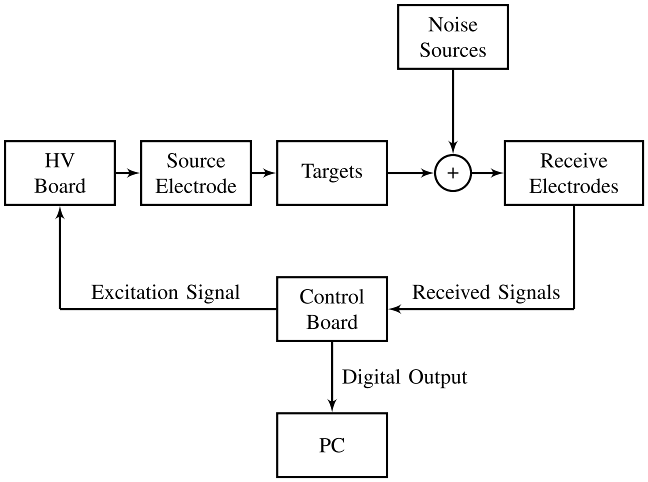

Fig. 1. Conceptual block diagram of the generalized standalone capacitive sensing system.

The circuitry consists of a high-frequency high-voltage (HV) source and differential receive electrodes with active amplification and common-mode feedback. These active receivers help to eliminate parasitic capacitance effects, which can dwarf the coupling capacitances, while the common-mode feedback eliminates line frequency (50 or 60 Hz) pickup, which can distort system measurements. Further, the source can accommodate multiple frequencies, which adds an independent dimension to the measurements, and the system is fully modular, as multiple source- and receive-pair electrodes. These capabilities combined make occupant localization a possibility.

The focus of this paper is an in-depth description of the circuitry comprising this capacitive sensing system. In Section II, an overview of the capacitive sensing system is given. Section III details the signal synthesis, amplification, and control systems comprising the HV signal source. Following that, Section IV describes the sensing circuitry of the active receiver system including the front-end signal amplification with common-mode feedback and the signal conditioning circuitry featuring synchronous detection and analog-digital conversion. Section V provides the results from performance tests of the system including detection range for a particular setup. In addition, this section shows the results of an initial investigation into occupant localization using a multisource single-receive-pair electrode setup. Finally, this paper concludes with a summary and a look forward to future research.

II. System Overview

A conceptual block diagram depicting the elemental sensor system is shown in Fig. 1. Each block represents an independent but interconnected subsystem. The control board contains circuitry that generates a low-voltage excitation signal. That signal is transmitted via a coaxial cable to the HV board for amplification and also into a source electrode via a coaxial cable. This electrode generates an electric field in the space being monitored. The targets present in the sensing space perturb the field and affect the coupling to two receive electrodes. These receive electrodes pickup the small currents capacitively coupled from the source electrodes and convert them via transimpedance amplifiers to voltage measurements. These sensed signals are then transmitted via a coaxial cable to the signal conditioning electronics back at the control board. The difference between the two signals is taken and then synchronously detected. This rectified signal is then low-pass filtered and fed to an analog-digital-converter (ADC). Finally, the digital output is passed to a computer via USB for data analysis and storage.

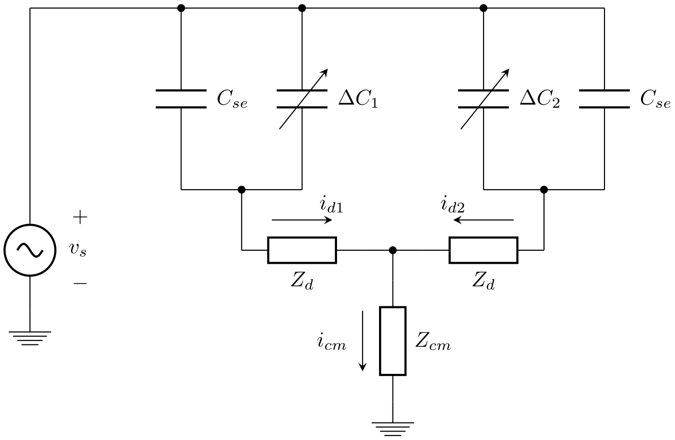

Fig. 2. Lumped element model for the capacitive sensor system.

A simplified lumped element small-signal electrical model for the sensor and environment system is shown in Fig. 2. The model depicts the dominant lumped capacitances of the system as two source-to-receive electrode capacitances C_{se}. In parallel with each of these capacitances are the variable capacitances from the source to the electrodes ΔC_1 and ΔC_2, which are dependent on the presence of an occupant. In general, these variable capacitances sensed by the system are significantly smaller than the fixed source-to-receive electrode capacitances. Previous work modeling building-scale capacitances provide approximate values for the model and were used in the design of this sensor [15], [21].

The measurement of interest is the differential current, $i_d = i_{d1} - i_{d2}$, i.e., the difference between the currents in each front-end amplifier modeled in Fig. 2 by their small-signal input impedance, Z_d. A common-mode feedback path described in more detail in Section IV drives each amplifier to a known potential and has some impedance path to the source ground through Z_{cm}. The common-mode feedback provides attenuation of the common-mode signal within the frequency range of source excitation, and thus, its path to the source ground is small.

To maximize the sensed current, Z_d and Z_{cm} should be minimized. In the limit that these impedances go to zero, the magnitude of the differential sensed current when the source voltage is sinusoidal is given by

$$|i_d| = |v_s|\omega(\Delta C_1 - \Delta C_2). \tag{1}$$

Here, $|v_s|$ is the magnitude of the source voltage and ω is the source voltage frequency.

While this model is an idealization as shunt capacitances to ground are ignored, (1) does reveal the general utility of the differential receiver subsystem. That is, the measurement of interest i_d depends only on the changes in capacitance and not the bulk capacitances of the space. Further, any common-mode pickup on the receivers within the frequency range of interest is cancelled by the differential measurement.

Also of note is that the system is quite modular. As is explained in Section III, the HV excitation signal can contain multiple frequency components. That is, the system supports multispectral imaging, which adds an independent dimension to the measurements as the permittivities of human materials, e.g., skin and muscle are frequency dependent [22]. Further, multiple voltage sources and/or multiple receiver pairs can be combined into a single system by multiplexing the transmitted and/or received signals on time. This is important in occupant localization applications.

III. HIGH-VOLTAGE SIGNAL SOURCE

To meet the operational requirements of the proposed application areas for this system, the HV signal source is designed to exhibit these specific features:

1) variable amplitude;
2) wide operating frequency range;
3) low noise floor;
4) low short-term and long-term drifts.

A. Signal Synthesis

The individual components of the HV excitation waveform are generated by AD9837 direct digital synthesis chips located on the control board. Each chip is controlled via a serial peripheral interface (SPI) from a local microcontroller. These chips use 10-b digital-to-analog converters along with other circuitry, e.g., memory and logic, to generate programmable sine waves at their outputs. Both frequency and phase offsets are controllable via the SPI bus allowing explicit optimization of the signal frequency content and intersignal phase relationships. The individual components are summed via an LT1806 operational amplifier (op-amp) with a preset gain, high-pass filtered with a first-order resistor–capacitor circuit, and then driven via coaxial cable to the HV circuit board via an LT1806 with proper impedance matching. For this paper, two discrete excitation frequencies were simultaneously included in the source signal at most, though the prototype system can accommodate up to four frequencies.

B. High Voltage Gain and Control

A circuit diagram and an accompanying control block diagram detailing the HV amplification scheme are shown in Fig. 3. The HV board receives the synthesized signal v_e and amplifies it to v_s over the course of several stages. Referring to Fig. 3(a), it can be seen that an AD8620 op-amp in a noninverting configuration first preamplifies the signal and allows the user to vary the overall system gain via the R_v potentiometer. Following this, the signal passes through an AD8620-based proportional integral (PI) controller followed by an OPA452 noninverting power op-amp driving a 9:1-turn autotransformer. The autotransformer allows the nonisolated output to be fedback via an RC network to the PI controller.

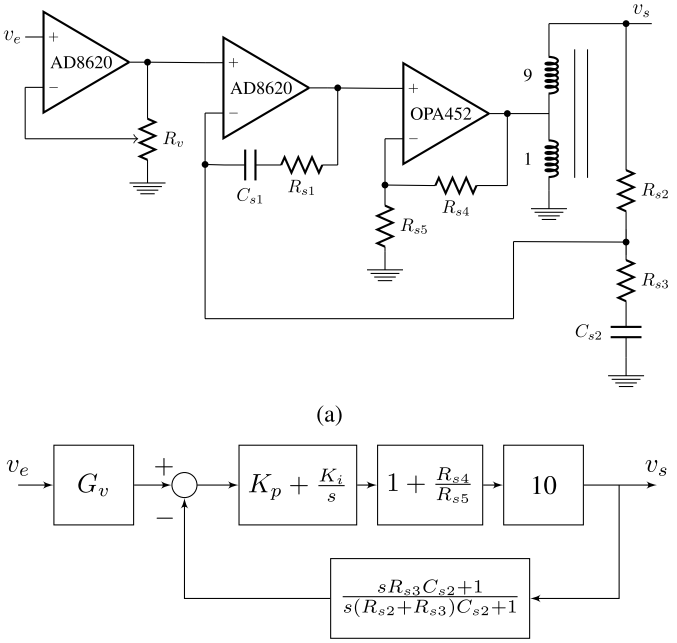

Fig. 3. (a) Simplified circuit model and (b) block diagram of the HV signal amplifying system.

The capacitor C_{s2} is included so that at dc, the feedback gain is unity and thus the overall system gain is approximately G_v. At the frequencies of excitation, however, this capacitor acts as a short, thus reducing the feedback signal through the voltage divider formed by R_{s2} and R_{s3}, and increasing the overall system gain. Designed for control at these frequencies, the PI controller parameters K_p and K_i are tuned via the resistor and capacitor relationships

$$K_p = \frac{R_p + R_{s1}}{R_p} \tag{2}$$

and

$$K_i = \frac{1}{R_p C_{s1}} \tag{3}$$

respectively. In these equations, $R_p = (R_{s2}R_{s3}/R_{s2} + R_{s3})$, i.e., the parallel combination of R_{s2} and R_{s3}.

In the prototype system built and used in testing, the proportional gain K_p was set to 2 and the integral gain K_i to 3×10^5. The resistors R_{s4} and R_{s5} were set equal so that the OPA452 amplifier had a dc gain of 2. This system was tested to be stable with a phase margin of 60.4° and a step response settling time of approximately 30 μs.

From the output of the autotransformer, the HV signal is driven via coaxial cable to a source electrode. The electrode itself is a two-plane FR4 printed circuit board (PCB) with active area dimensions of 15 cm × 21 cm. Both planes serve as the active electrode with a grid of vias spaced at 1.25-cm increments serving to electrically connect both planes. A picture of a receiver electrode, which is identical to the source electrode except for the additional front-end amplifier circuitry, is shown in Fig. 5. Overall, the source system can generate an HV signal at the source electrode with a maximum amplitude of 500 V and a bandwidth of 10–100 kHz.

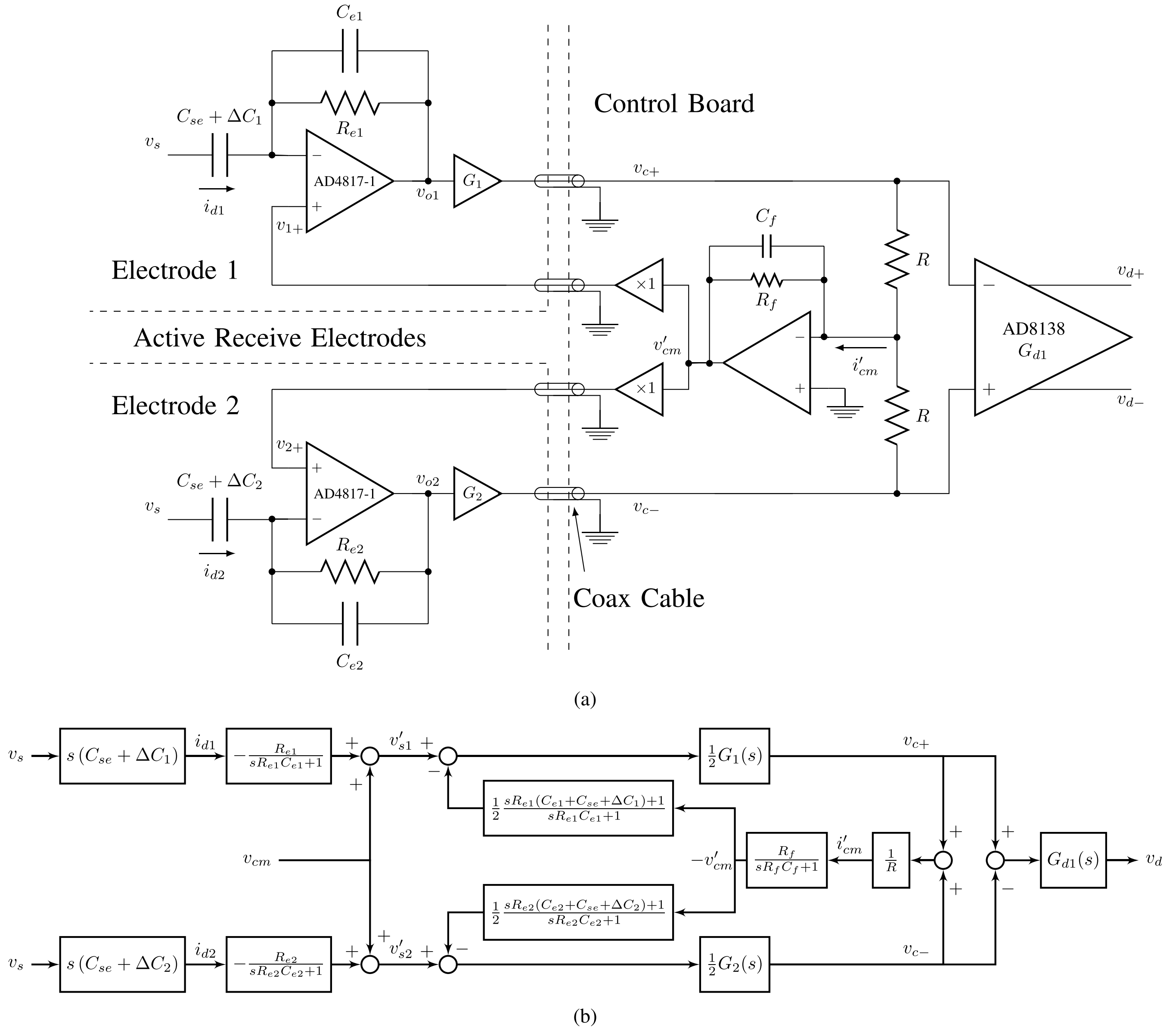

(a)

(b)

Fig. 4. (a) Schematic and (b) functional block diagram of the front-end differential amplifier system. Electrode circuitry is to the left of the cables and sensor board circuitry is to the right in (a).

IV. SENSING CIRCUITRY

As described in Section II, the measurements of interest are the capacitively coupled currents at the receive electrodes. A front-end amplifier system distributed between the active receiver electrodes and the control board converters is employed to detect these currents, subtract the two, and add gain. This differential signal is then passed to a signal conditioning circuit, which synchronously rectifies the signal and converts the analog signal to digital values for subsequent software analysis and storage.

A. Front-End Amplifier

Fig. 4 shows the circuit schematic and functional block diagram for the front-end amplifier system with common-mode feedback. Each receiver electrode contains a single-ended transimpedance amplifier locally which converts the current inputs, i_{d1} and i_{d2}, into voltage signals, v_{o1} and v_{o2}, respectively. These signals are then further amplified by non-inverting op-amps with gains $G_1(s)$ and $G_2(s)$, respectively. For the purposes of the discussion here, these gains are lumped terms combining the ideal gain of the op-amps, plus errors due to component inaccuracies and system parasitics. The resulting voltage signals are then driven via coaxial cable to the control board where the difference between the two signals, $v_d = v_{c+} - v_{c-}$, is taken.

1) Active Receive Electrodes: An example receiver electrode is shown in Fig. 5. The electrode is of the same construction as the source electrode except for the front-end amplifier, which is located in the top-left corner of the board. This sensing node is one of the most sensitive points in the system. Constraining it to the receive electrode helps to

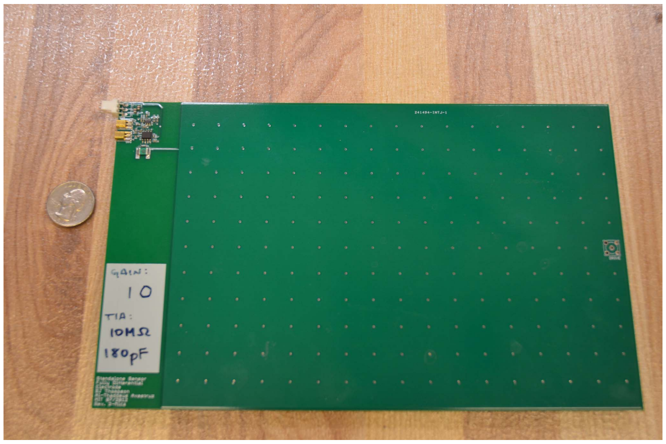

Fig. 5. Each receive electrode has an active area of 15 cm × 21 cm. The circuitry at the very top left of the electrode is a front-end transimpedance amplifier for active delivery of the sensed signal to the control board. Image reused with permission from [17].

avoid parasitic capacitances, reduces the potential to pick up extraneous signals from noise sources, and limits interference from the environment.

The front-end transimpedance amplifier intrinsically acts as the first gain stage of the sensing circuitry. Taking electrode 1 as an example and restricting the analysis to frequencies less than the bandwidth of the op-amp, the transimpedance amplifier has a transfer function given by

$$\frac{v_{o1}}{i_{d1}} = -\frac{R_{e1}}{sR_{e1}C_{e1}+1}. \tag{4}$$

With the input current provided by the signal source and the source-to-receive plate capacitance such that $i_{d1} = v_s s(C_{\text{se}} + \Delta C_1)$, then the front-end source voltage to op-amp output voltage gain is

$$G_{\text{fe1}} = -\frac{sR_{e1}(C_{\text{se}}+\Delta C_1)}{sR_{e1}C_{e1}+1}. \tag{5}$$

From (5), there are two general modes of operation. For source frequencies, $\omega_s < (1/R_{e1}C_{e1})$, the transimpedance amplifier acts as a differentiator with gain proportional to signal frequency. This is attractive as the system gain can be increased simply by increasing source frequency. For $\omega_s > (1/R_{e1}C_{e1})$, the gain is the constant ratio, $(C_{\text{se}} + \Delta C_1)/C_{e1}$, which is attractive for multifrequency operation as the system sensitivity is consistent for all source components. Further, to maximize system gain in this region, C_{e1} should be minimized, though that requires an increase in R_{e1} to maintain the frequency range of this region. An equivalent analysis also applies for electrode 2 with the front-end gain

$$G_{\text{fe2}} = -\frac{sR_{e2}(C_{\text{se}}+\Delta C_2)}{sR_{e2}C_{e2}+1}. \tag{6}$$

In this paper, a multifrequency source was employed with frequency components in the 10–100 kHz range. As such, C_{e1} and C_{e2} had ideal values of 180 pF, and R_{e1} and R_{e2} had ideal values of 10 MΩ so that these frequency components were well within the constant gain range.

2) Common-Mode Feedback: The main sources of interference in this system are the utility pickup (typically 50 or 60 Hz) and the electric fields from any surrounding fluorescent lamp ballasts, which typically switch around 50 kHz. These signals are problematic as their additive nature reduces the headroom in the sensing circuitry prior to the synchronous detection. To reduce the system's susceptibility to these components, a common-mode feedback path is employed to drive the noninverting inputs of the two front-end amplifiers and null any common-mode signals.

Again referring to Fig. 4(a), it can be seen that the outputs of the electrodes are sent via coaxial cable to the sensor board where the common-mode signal is taken from the midpoint of two resistors, each shown as R. The common-mode signal is then passed through a low-pass configured op-amp circuit. The output of this op-amp then drives the noninverting input of the front-end amplifiers. The block diagram of Fig. 4(b) is useful for analyzing the benefit of the common-mode feedback. Here, signals v'_{s1} and v'_{s2} represent composite signals at the electrodes composed of the desired signal plus common-mode interference signals. Considering the lumped gain terms as containing an ideal component plus a gain error, i.e., $G_1(s) = G(s) + \Delta G_1(s)$ and $G_2(s) = G(s) + \Delta G_2(s)$, then without the feedback, the system's differential output is given by

$$v_d = A'_d(v'_{s1} - v'_{s2}) + A'_{\text{cm}}\left(\frac{v'_{s1}+v'_{s2}}{2}\right) \tag{7}$$

with the differential gain, $A'_d = (1/2)G_{d1}(s)G(s)$, and the common-mode gain, $A'_{\text{cm}} = G_{d1}(s)(\Delta G_1(s) - \Delta G_2(s))$. Here, the (1/2) terms come from impedance matching in signal transmission between the electrodes and control boards, and $G_{d1}(s)$ is the additional gain configured on the AD8138 differential op-amp.

The feedback loops of Fig. 4 are designed to reduce A_{cm} over the frequencies of interference. Under normal operation, $C_{e1} \gg C_{\text{se}} + \Delta C_1$ and $C_{e2} \gg C_{\text{se}} + \Delta C_2$, and the common-mode feedback for each electrode, $H(s) = (v_{1+}/v_{c+} + v_{c-}) = (v_{2+}/v_{c+} + v_{c-})$, reduces to

$$H(s) = \frac{1}{2}\frac{R_f}{R}\frac{1}{sR_fC_f+1}. \tag{8}$$

Again, the (1/2) term comes from impedance matching across the coax cables.

With this common-mode feedback, the differential signal output becomes

$$v_d = A_d\left(v'_{s1} - v'_{s2}\right) + A_{\text{cm}}\left(\frac{v'_{s1}+v'_{s2}}{2}\right) \tag{9}$$

with

$$A_d = A'_d\frac{1 + G(s)H(s)\left(1+\frac{\Delta G_1(s)}{G(s)}\right)\left(1+\frac{\Delta G_2(s)}{G(s)}\right)}{1+G(s)H(s)\left(1+\frac{\Delta G_1(s)+\Delta G_2(s)}{2G(s)}\right)} \tag{10}$$

and

$$A_{\text{cm}} = \frac{A'_{\text{cm}}}{1+G(s)H(s)\left(1+\frac{\Delta G_1(s)+\Delta G_2(s)}{2G(s)}\right)}. \tag{11}$$

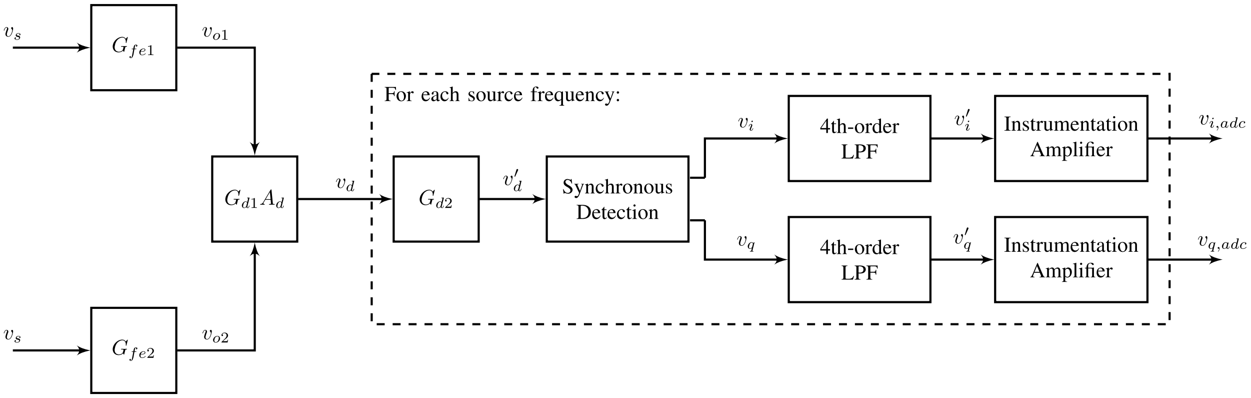

Fig. 6. Generalized block diagram for the signal conditioning circuitry. The stages in the dashed-box are fully differential and are replicated for each frequency component of interest in the source signal.

Thus, when $G(s)H(s) \gg 1$, A_{cm} is significantly attenuated from A'_{cm}, while $A_d \approx A'_d$ so long as $\Delta G_1(s)$ and $\Delta G_2(s)$ are small compared with $G(s)$. For the prototype system utilized in this paper, the ideal forward gain was set to $G(s) = 10$, the differential gain $G_{d1}(s) = 10$, and the common-mode feedback components were set as $R = 10$ kΩ, $R_f = 1$ MΩ, and $C_f = 2$ pF. In accordance with (8) and (11), this ensures a common-mode attenuation of approximately −60 dB over the frequency range 0–80 kHz, which covers the typical highest energy interference components.

B. Signal Conditioning

Following initial signal sensing, the signal conditioning circuitry adds further gain and converts the differential analog signal to a digital representation for software analysis and storage. A block diagram describing the general operation of the signal conditioning circuitry is depicted in Fig. 6. The sensed differential signal v_d is further amplified through an additional cascaded AD8138 with a gain of G_{d2}. Because the presence and movement of a person in the room effectively modulates the capacitively coupled currents at the electrode, v'_d is passed through a synchronous demodulation circuitry, which generates signals, v_i and v_q, containing the in-phase and quadrature components of v'_d, respectively. These signals are then low passed via a fourth-order filter to remove higher order terms. Finally, instrumentation amplifiers are used to impart the final amplification while also level shifting the signals for passing to a 24-b ADC controlled by the microcontroller unit.

Each frequency component contained in the source signal v_s requires its own circuitry. As such, the prototype system developed here repeats the portion of the block diagram inside the dashed box for each signal frequency component. It is also important to note that at each stage of the signal conditioning circuitry, signal processing is kept fully differential to continue minimizing signal interference from external sources.

V. APPLICATION PERFORMANCE TESTING

Several tests were performed to demonstrate and quantify the system's utility. Specifically, two capacitive sensing configurations based on the system described above were constructed for occupancy detection and occupancy localization applications. These particular configurations are not necessarily optimal; additional research is ongoing toward configuration optimality [23], however, they serve to illustrate the potential for long-range capacitive sensing applications.

A. Single-Source System

For initial testing and demonstration, a single-source system was constructed in a planar fashion with the source electrode placed between the two receive electrodes as shown in Fig. 7. Here, Fig. 7(a) shows the two receive electrodes to the left and right and at a slightly lower level from the source electrode, which is covered in electrical tape for safety purposes. The control board is located below the source electrode. This sort of planar setup, i.e., where the source- and receive-pair electrodes are located in a single plane, might be useful in detecting occupancy through a wall in a room or hallway. The electrodes could be inconspicuously incorporated into the building structure, e.g., behind drywall, and still effectively detect occupancy as the thin drywall and its associated conductivity and permittivity have little effect on the electric field distribution in the room. In this configuration, however, care must be taken to ensure conductive materials, e.g., metallic framing, sewage pipes, and electrical distribution wires are kept away from the electrodes.

The illustration of Fig. 7(b) depicts two paths walked by a male subject, Person A, approximately 1.8 m (5.75 ft) tall and 77 kg (170 lbs) in weight. In the first path (shown by the vertical arrow), the subject walked in steps 0.25 m in length from left to right across the sensor setup at a distance of 2 m away. This test was done to illustrate the characteristic response shape as a person moves one-dimensionally through a space. The second path (shown by the horizontal arrow) was walked to test the range of the system configuration. For this test, the same subject began the path directly in front of the right receive electrode 0.25 m away from the sensor setup and walked perpendicularly away in increments of 0.25-m steps until 5 m from the sensor setup. For all tests, a single-source frequency of 10.4 kHz was utilized with each path being walked a total of five times corresponding to different levels of source voltage magnitude.

(a) System Configuration

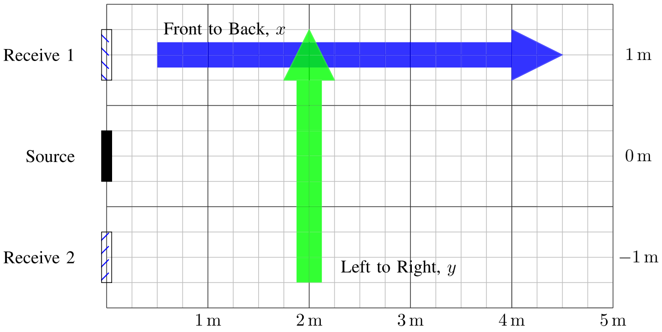

(b) Testing Paths

Fig. 7. Single-source planar setup for occupant detection testing. (a) Image of the system setup. (b) Testing paths walked during testing.

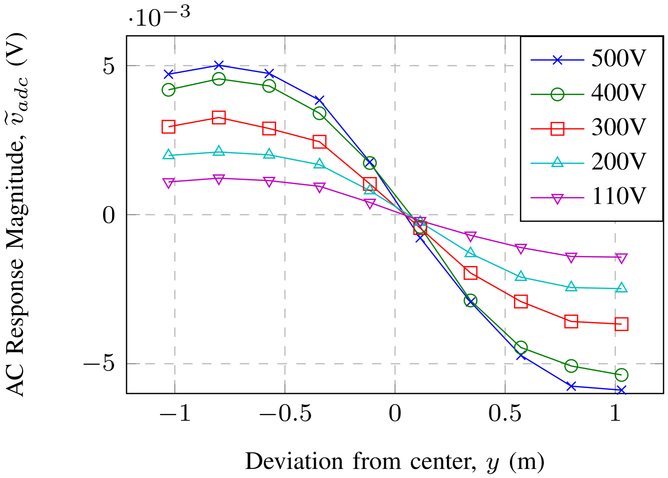

Fig. 8. Measured responses for person movement from left to right with varied source amplitudes.

To generate the results shown here, measurements were taken every 2 s to allow the subject to ensure that his location is the same for corresponding measurements between tests. Thus, the performance of the transmitter–receiver system was not specifically tested to account for the pace of the subjects' gait. However, the rate-limiting subsystem [fourth-order low-pass filter following the synchronous demodulation (Fig. 6)], has a 95% settling time of approximately 18 ms. To put this settling time into perspective, a person with a fast gait travels approximately 1.6 m/s [24]. If such a person walked across the 5-m measurement area at that speed, the transmitter–receiver system could accommodate 170 samples, which is more than sufficient for detecting an occupant. This analysis does not account for the effects of noise and disturbances inherent in the measurement space.

Fig. 8 shows a plot of the ac response magnitude $\widetilde{v}_{\text{adc}}$, where $|v_{\text{adc}}| = (v_{i,\text{adc}}^2 + v_{q,\text{adc}}^2)^{1/2}$ and $\widetilde{v}_{\text{adc}} = |v_{\text{adc}}| - \overline{|v_{adc}|}$. Here, $\overline{|v_{adc}|}$ indicates the mean magnitude. Fig. 8 shows that there is a clear change in the signal response as the subject moves through the room, with the response magnitude roughly increasing linearly with source magnitude (labeled in the figure legend). Knowledge of this characteristic response could be used to sense an occupant's movement along a 1-D path, e.g., a hallway. Of note, however, that there is a null space along this path when the occupant is in line with the source due to symmetry in the room. Thus, for true occupancy detection, a second (or more) source and/or receiver pair is required to break the symmetry of the measurement space. For example, an equivalent source- and receiver-pair systems could be setup on the opposing side of the measurement space and achieve true occupant detection so long as the second system is offset from the first along the y-axis (Fig. 7).

Fig. 9 shows the results of the test where the subject moved from near to far from the sensor system. Again, the source voltage magnitude corresponding to each test is given in the figure legends. Here, Fig. 9(a) depicts the response magnitude, while Fig. 9(b) illustrates the change in response magnitude between data points and normalized by the step distance (0.25 m). As expected, larger source voltages yield larger signal responses as shown in Fig. 9(a) and thus increase the sensitivity of the system. The large dip in response seen when the subject is roughly 0.5 m from the sensor system is due to the fact that when very close to the system, the subject acts as a path to complete the electric field between the two electrodes [25]. As the subject moves away from the system, the person begins to act as a path to shunt the electric field to ground instead, thus abruptly decreasing the capacitive coupling and hence the dip in response magnitude. However, as the person continues to walk away from the electrode, the person's effect on the electric field decreases to zero and the capacitive coupling increases again. While not investigated in this paper, this effect is directly due to the presence of a person and as such could be exploited for occupancy localization and interfacing.

Fig. 9(b) gives insight into the effective range of the sensor circuitry for this given particular configuration. Specifically noting the 500 V source response, between around 1 and 3.5 m, the change in the response between data points is exponentially related to the subject distance from the sensor. After 3.5 m, the response is relatively flat even as the subject continues to move away. This indicates that the influence that the subject has on the system is no longer detectable above the noise floor. Thus, the range for the 500 V source is around 3.5 m. This performance decreases as the source

This article has been accepted for inclusion in a future issue of this journal. Content is final as presented, with the exception of pagination.

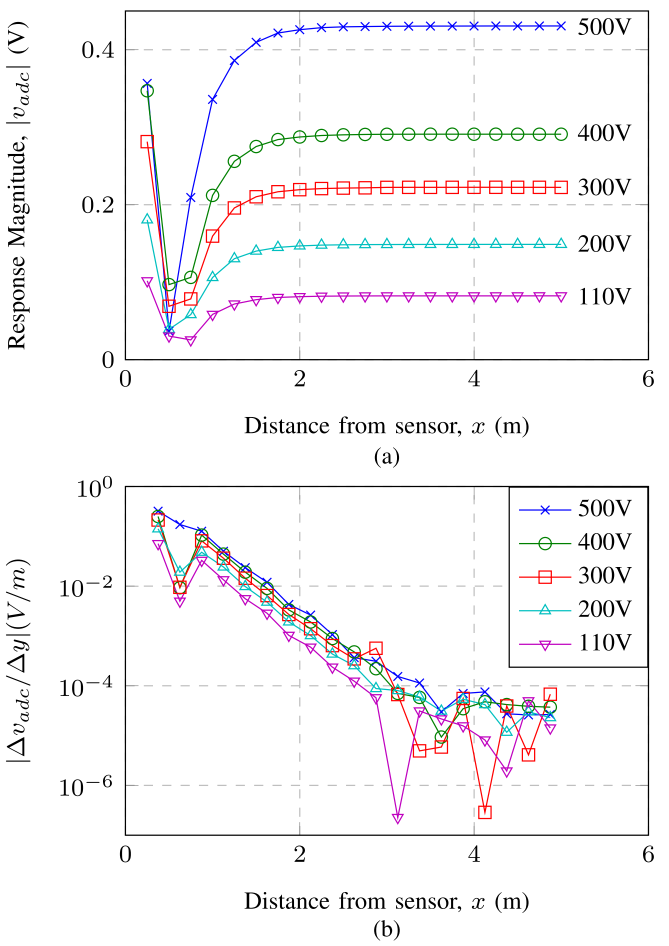

Fig. 9. (a) Measured response and (b) change in response as functions of distance away from one sensor.

voltage decreases though even for a voltage of only 110 V, the range is still roughly 3 m.

While not shown here, tests with other subjects of different heights and weights (and thus, surface area and volume [26]) revealed that the magnitude of the response is also affected by the size and shape of the occupant. For example, a female subject, Person B, approximately 1.65 m (5.42 ft) and 52 kg (115 lbs) traversing the left-to-right path generated a very similar response to that of Fig. 8 but with a magnitude 40%–50% smaller than the first occupant. Thus, there are some implications on system range and accuracy dependent on human variations, but this was not explicitly studied in evaluating this prototype system.

B. Multisource System for 2-D Occupancy Detection and Localization

A multisource system based on the modular single-source system described in Sections III and IV was setup in accordance with Fig. 10. Here, three source electrodes, labeled s_1, s_2, and s_3 in Fig. 10, were placed on one side of the detection space approximately 1.3 m apart at a height of 1 m above the floor. The differential receive electrode pair, labeled r_1 and r_2, was located 3.2 m across the space, 2.7 m apart, and also 1 m above the floor. For this test, the detection space was divided into a 4×4 grid, with each pixel approximately 0.8 m $\times$ 0.8 m in size. Again, this configuration is not necessarily optimal.

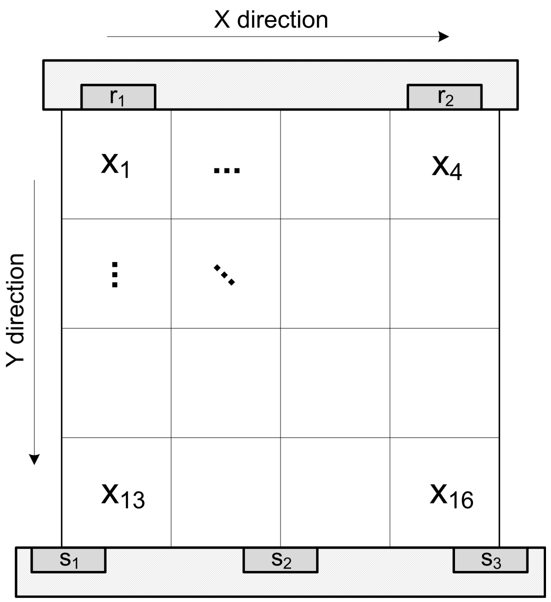

Fig. 10. Conceptual diagram of the 4 × 4 grid used to test 2-D occupancy detection. Each square represents a pixel in the space.

During testing, two frequency components were included in the source signal, one at 10.4 kHz and one at 83.3 kHz. These frequencies were chosen as the dielectric properties of the human tissue vary over this frequency range [22] allowing independent measurements at the two frequencies. The three sources were multiplexed in time so that only one source was ON at a given time. Thus, for a complete scan of the space, 12 measurements were passed to the ADC, i.e., $v_{i,\text{adc}}$ and $v_{q,\text{adc}}$, as shown in Fig. 6, for both frequencies and each source plate.

1) Occupancy Model: Taking inspiration from electrical impedance tomography and image processing applications [27]–[29], the processing method for detecting and localizing an occupant in this space was formulated as solving the linear equation

$$\mathbf{S}\boldsymbol{x} = \boldsymbol{v} \tag{12}$$

for $\boldsymbol{x}$ in the least-norm sense and in accordance with an image segmentation algorithm (Algorithm 1). In (12), $\mathbf{S}$ is an $m \times n$ sensitivity matrix calibrated to the space and sensor setup, $\boldsymbol{x}$ is an $n \times 1$ occupancy vector, and $\boldsymbol{v}$ is an $m \times 1$ column vector. n corresponds to the number of pixels in the space and m to the number of measurements during a complete scan. For the system of Fig. 10, $n = 16$ and $m = 12$. Thus, this system is underdetermined and an infinite set of occupancy vectors exist, which satisfy (12).

To prioritize an occupancy vector solution $\hat{\boldsymbol{x}}$ with meaningful component values, a segmentation algorithm was employed that relies on iteratively partitioning the space into quadrants and solving the corresponding partitioned portion of (12) by selecting $\hat{\boldsymbol{x}}_q$, which is given by

$$\begin{aligned}&\text{Min: } ||\mathbf{S}_q\hat{\boldsymbol{x}}_q - \hat{\boldsymbol{v}}_q||_1 + \lambda||\hat{\boldsymbol{x}}_q||_1\\ &\text{s.t. } \hat{\boldsymbol{x}}_q \geq 0 \quad \text{and } 0 \leq \lambda < 1.\end{aligned} \tag{13}$$

Algorithm 1 Space Segmentation Algorithm With Least-Norm Optimization

```
1: Subdivide space into quadrants $Q = \{q_1, q_2, q_3, q_4\}$
2: for Each $q \in Q$ do
3:   Find partitioned-system least-norm solution, $\hat{\boldsymbol{x}}_q$
4:   Find energy of each solution, $E(\hat{\boldsymbol{x}}_q)$
5:   if Energy in $q$ is insignificant compared to average then
6:     Quadrant $q$ is unoccupied, and set $\hat{\boldsymbol{x}}(q) = \mathbf{0}$
7:   else
8:     Quadrant $q$ is occupied, and
9:     if $q$ is a single pixel then
10:      Set $\hat{\boldsymbol{x}}(q) = \hat{\boldsymbol{x}}_q$
11:    else
12:      Subdivide $q$ into quadrants, and repeat lines 2-15
13:    end if
14:  end if
15: end for
16: return $\hat{\boldsymbol{x}}$
```

Here, q represents a specific partitioning of the space and corresponding partition of (12), e.g., quadrant I of the full test space includes pixels 3, 4, 7, and 8 (Fig. 10).

The 1-norm for minimization was selected over the 2-norm (least squares) as the 1-norm is more robust to outliers since the cost function of (13) grows linearly rather than quadratically with errors [30]. In addition, the 1-norm penalty with weighting term λ adds stability to the inverse problem while also aiding to favor sparsity [30]–[32] in the solution. This is characteristic of the capacitive sensing system in most situations, i.e., when a space is occupied by a couple of subjects at a given time at most. Finally, the occupancy vector $\hat{\boldsymbol{x}}$ is further constrained to be positive as negative occupancy does not have a physical meaning in the model.

The employed algorithm is summarized in Algorithm 1. The method starts by dividing the test space into four quadrants. For each quadrant, a solution $\hat{\boldsymbol{x}}_q$ is found in accordance with (13) and the energy of each quadrant is calculated as

$$E(\hat{\boldsymbol{x}}_q) = \|\hat{\boldsymbol{x}}_q\|_2^2. \tag{14}$$

If the energy in a specific quadrant is insignificant compared with the average energy in all quadrants

$$E(\hat{\boldsymbol{x}}_q) <= \epsilon \frac{1}{4} \sum_{Q} E(\hat{\boldsymbol{x}}_q) \tag{15}$$

then, the quadrant is deemed unoccupied and its corresponding partition of the overall occupancy vector $\hat{\boldsymbol{x}}(q)$ is set to $\mathbf{0}$. Here, ϵ represents a significance factor, which increases image sparsity as its value increases.

On the other hand, if there is sufficient energy in a quadrant's solution, the algorithm deems the quadrant as occupied. If q corresponds to just a single pixel, then the overall solution vector is updated to contain the value for that particular pixel, i.e., $\hat{\boldsymbol{x}}(q) = \hat{\boldsymbol{x}}_q$. Finally, if q contains more than a single pixel, the algorithm subdivides q into its quadrants and the process is repeated for this system subspace.

2) Detection and Localization Testing: To calibrate the sensitivity matrix, measurements were taken during single pixel occupation and $\boldsymbol{x}$ set such that the kth element $x_k = 1$ when the kth pixel was occupied and all other elements were set to 0. In this way, the kth column of $\mathbf{S}$ is equal to the measurement vector v. This calibration was performed with the same human subject (Person A) as that utilized for the tests of Figs. 7–9.

Testing was then performed to test the algorithm's ability to detect a true negative, i.e., no occupant in the measurement space and a true positive, i.e., when Person A only occupies the space. In addition, a second person (Person B as described previously) of smaller height, weight, and corresponding surface area and volume was introduced into the space to test detecting and localizing the position of the two individuals simultaneously. Similar to the single-source tests, individual pixel measurements were collected every 2 s to ensure the location of the subject. Given the constraints of the system, however, and again not accounting for effects of background noise on measurement accuracy, the system has an ability to measure pixel occupancy in approximately 60 ms. Again, the rate limiting subsystem is the low-pass filter of the signal conditioning chain; however, now the system must accommodate three settling times of 18 ms as each source is switched ON–OFF in each cycle.

In this manner, the capacitive sensing system and detection algorithm proved reasonably useful in detecting occupants provided they stayed near the edges of the room and well separated in the space. That is, the algorithm was unable to reliably detect single person occupancy or multiperson occupancy when the subjects occupied the middle pixels. Fig. 11 shows occupancy reconstruction images representative of the results achieved for these given conditions. Here, Fig. 11(a) shows the recovered occupancy image when there is no subject in the measurement space, while Fig. 11(b) shows that when the person used to calibrate the space, Person A, is occupying pixel 1. In both these cases, the algorithm correctly identifies the occupancy in the room and returns an occupancy near 1 when just Person A is in pixel 1.

Fig. 11(c) shows the recovered occupancy image when the subject used to calibrate the space, Person A, is occupying pixel 1, while Person B is occupying pixel 16, while Fig. 11(d) shows that when their locations are switched. In both cases, the algorithm is able to isolate single pixel occupation and is even able to differentiate between the two people. That is, the pixels occupied by Person A contains a higher occupancy value [0.8 and 0.48 for Fig. 11(c) and (d), respectively] than those occupied by Person B (0.35 and 0.3, respectively). This is consistent with Person A being of larger mass, height, and surface area than Person B and as such imparts a larger variation in capacitive coupling between the sources and receivers.

During testing when either of the occupants were in the center four pixels or located in close proximity, results were inconsistent with the algorithm at times missing occupation locations or producing incorrect occupation. This is likely due to a combination of notable factors. First, the measurement system is less sensitive to changes in occupancy near the center of the testing space as occupants are relatively far from both

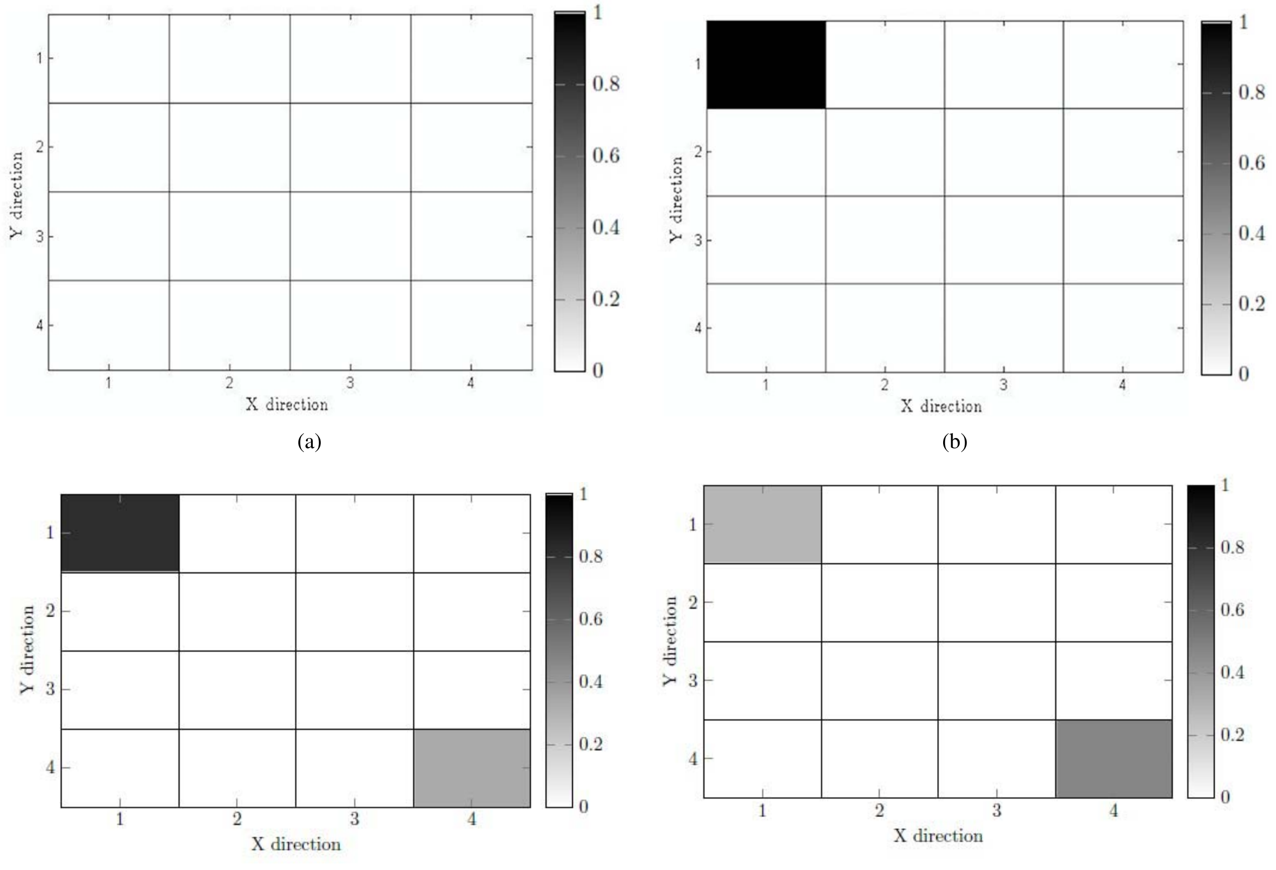

(a)

(b)

(c)

(d)

Fig. 11. Occupancy values in a 4 × 4 gridspace with two people differentiated by size. (a) No occupant in the grid. (b) Person A in pixel 1. (c) Person A in pixel 1 and Person B in pixel 16. (d) Person B in pixel 1 and Person A in pixel 16.

the sources and the receivers. This decreased sensitivity results in a smaller signal-to-noise ratio and errors in the calibrated sensitivity matrix $\mathbf{S}$ and each collected measurement vector $\boldsymbol{v}$. Second, the system model defined in (12) is linear, but changes in capacitive coupling due to the presence of two occupants increase in nonlinearity as the two occupants move closer together.

Both of these factors can result in the least-norm solutions (13) having misallocated occupancy energy or widely distributed energy (not sparse). This combined with the all-or-nothing approach of the algorithm, i.e., occupancy is defined only on the singular pixel level and only energy values above a threshold result in positive occupancy assignments, can result in the incorrectly assigned occupancy and missed occupancy assignments observed during testing.

VI. CONCLUSION

The circuitry presented in this paper comprises a novel long-range capacitive sensing system featuring a standalone signal source and differential pair active receiver electrodes. During performance tests of the system aimed to quantify its utility in human occupancy detection, the system showed a detection range of approximately 3.5 m. Further, the system supports multifrequency electric fields and is modular as multiple source electrodes can be combine with multiple differential pair receiver electrodes. When combined with an image segmentation algorithm, these functionalities showed the system's potential for human occupancy localization.

This capacitive sensing platform has many potential applications. An elemental system can function as a room occupancy detector important in smart building systems such as HVAC and lighting. Importantly, this capacitive sensing system does not suffer from the high-pass nature of the commonly used PIR or ultrasonic sensors, which ultimately limits them to motion detection [19], [20].

When multiple systems are combined, the capacitive sensor network supports occupancy localization, which could be used to track room occupants as part of security systems or to detect falls as part of assisted living monitors. Further, the system can be used as a platform for investigating the incorporation of capacitive sensing systems into standard building materials. For example, the PCB-based electrodes could be incorporated into ceiling or floor tiles or be replaced all together using conductive paints on walls or ceilings. In addition, the multifrequency source components provide the possibility of material detection as materials have unique permittivity–frequency relationships. This concept potentially could be further extended by utilizing spread spectrum methods for increased resolution in the frequency domain as well as reduced susceptibility to narrow band interference, e.g., switching power supplies and lighting ballasts.

It should be acknowledged that this prototype system requires voltages that could present safety hazards. Future iterations of the system will investigate incorporating higher frequency excitation signals, which would allow source voltages to decrease. That is, the sensed signals are the capacitively coupled currents, which are derivative terms of the source voltage components. Since these source voltages are sinusoidal in nature, their derivatives are scaled in magnitude by the signal frequency and increasing frequency increases the picked-up signal without increasing source voltage. Still, the current system can be made safe by following safety design guidelines for standard building items with similar or higher voltages, such as florescent lamp ballasts or microwave transformers.

ACKNOWLEDGMENT

The authors would like to thank Prof. P. Marpu for the valuable advice and assistance.

REFERENCES

[1] L. K. Baxter, *Capacitive Sensors: Design and Applications*. New York, NY, USA: Wiley, 1997. [Online]. Available: http://ieeexplore.ieee.org/xpl/articleDetails.jsp?arnumber=5312316

[2] G. Brasseur, "Design rules for robust capacitive sensors," *IEEE Trans. Instrum. Meas.*, vol. 52, no. 4, pp. 1261–1265, Aug. 2003.

[3] T.-H. Hwang, W.-H. Cui, I.-S. Yang, and O.-K. Kwon, "A highly area-efficient controller for capacitive touch screen panel systems," *IEEE Trans. Consum. Electron.*, vol. 56, no. 2, pp. 1115–1122, May 2010.

[4] J. Lee, M. T. Cole, J. C. S. Lai, and A. Nathan, "An analysis of electrode patterns in capacitive touch screen panels," *J. Display Technol.*, vol. 10, no. 5, pp. 362–366, May 2014.

[5] F. Aezinia, Y. Wang, and B. Bahreyni, "Three dimensional touchless tracking of objects using integrated capacitive sensors," *IEEE Trans. Consum. Electron.*, vol. 58, no. 3, pp. 886–890, Aug. 2012.

[6] F. Aezinia, Y. Wang, and B. Bahreyni, "Touchless capacitive sensor for hand gesture detection," in *Proc. IEEE Sensors*, Oct. 2011, pp. 546–549.

[7] M. Howing, "Seat occupant detection system," U.S. Patent 5 525 843, Jun. 11, 1996. [Online]. Available: https://www.google.com/patents/US5525843

[8] B. George, H. Zangl, T. Bretterklieber, and G. Brasseur, "Seat occupancy detection based on capacitive sensing," *IEEE Trans. Instrum. Meas.*, vol. 58, no. 5, pp. 1487–1494, May 2009.

[9] B. George, H. Zangl, T. Bretterklieber, and G. Brasseur, "A combined inductive–capacitive proximity sensor for seat occupancy detection," *IEEE Trans. Instrum. Meas.*, vol. 59, no. 5, pp. 1463–1470, May 2010.

[10] A. S. Zeeman, M. J. Booysen, G. Ruggeri, and B. Lagana, "Capacitive seat sensors for multiple occupancy detection using a low-cost setup," in *Proc. IEEE Int. Conf. Ind. Technol. (ICIT)*, Feb. 2013, pp. 1228–1233.

[11] B. George, H. Zangl, and T. Bretterklieber, "A warning system for chainsaw personal safety based on capacitive sensing," in *Proc. IEEE Sensors*, Oct. 2008, pp. 419–422.

[12] B. Pottier, L. Rasolofondraibe, and D. Nuzillard, "A novel capacitive safety device for target localization and identification," *IEEE Sensors J.*, vol. 8, no. 10, pp. 1640–1647, Oct. 2008.

[13] B. Pottier and L. Rasolofondraibe, "Capacitive sensor dedicated to pedestrians protection," *IEEE Sensors J.*, vol. 15, no. 10, pp. 5886–5892, Oct. 2015.

[14] W. Buller and B. Wilson, "Measurement and modeling mutual capacitance of electrical wiring and humans," *IEEE Trans. Instrum. Meas.*, vol. 55, no. 5, pp. 1519–1522, Oct. 2006.

[15] J. J. Cooley, A. T. Avestruz, and S. B. Leeb, "A retrofit capacitive sensing occupancy detector using fluorescent lamps," *IEEE Trans. Ind. Electron.*, vol. 59, no. 4, pp. 1898–1911, Apr. 2012.

[16] A.-T. Avestruz, J. J. Cooley, D. Vickery, J. Paris, and S. B. Leeb, "Dimmable solid state ballast with integral capacitive occupancy sensor," *IEEE Trans. Ind. Electron.*, vol. 59, no. 4, pp. 1739–1750, Apr. 2012.

[17] W. H. Thompson, "A standalone capacitively coupled occupancy sensor," M.S. thesis, Dept. Elect. Eng. Comput. Sci., Massachusetts Inst. Technol., Cambridge, MA, USA, Sep. 2012.

[18] E. C. George, "Advanced applications in wide-area impedance sensing," M.S. thesis, Dept. Elect. Eng. Comput. Sci., Massachusetts Inst. Technol., Cambridge, MA, USA, Feb. 2014.

[19] Z. Zhang, X. Gao, J. Biswas, and J. K. Wu, "Moving targets detection and localization in passive infrared sensor networks," in *Proc. 10th Int. Conf. Inf. Fusion*, Jul. 2007, pp. 1–6.

[20] M. Levy, "Low-cost occupancy sensor saves energy," *Atmel Appl. J.*, no. 3, pp. 11–12, Summer 2004.

[21] J. J. Cooley, "Analysis, modeling and design of energy management and multisource power systems," M.S. thesis, Dept. Elect. Eng. Comput. Sci., Massachusetts Inst. Technol., Cambridge, MA, USA, Jun. 2011.

[22] S. Gabriel, R. W. Lau, and C. Gabriel, "The dielectric properties of biological tissues: II. Measurements in the frequency range 10 Hz to 20 GHz," *Phys. Med. Biol.*, vol. 41, no. 11, p. 2251, 1996.

[23] B. Sennett, "Opportunities for human-interfaced capacitive sensing in building environments," M.S. thesis, Dept. Elect. Eng. Comput. Sci., Massachusetts Inst. Technol., Cambridge, MA, USA, Feb. 2015.

[24] T. Oberg, A. Karsznia, and K. Oberg, "Basic gait parameters: Reference data for normal subjects, 10–79 years of age," *J. Rehabil. Res. Develop.*, vol. 30, no. 2, pp. 210–223, 1993.

[25] J. Smith, T. White, C. Dodge, J. Paradiso, N. Gershenfeld, and D. Allport, "Electric field sensing for graphical interfaces," *IEEE Comput. Graph. Appl.*, vol. 18, no. 3, pp. 54–60, May 1998.

[26] J. Sendroy, Jr., and H. A. Collison, "Determination of human body volume from height and weight," *J. Appl. Physiol.*, vol. 21, no. 1, pp. 167–172, Jan. 1966.

[27] W. Q. Yang and L. Peng, "Image reconstruction algorithms for electrical capacitance tomography," *Meas. Sci. Technol.*, vol. 14, no. 1, pp. R1–R13, Jan. 2003.

[28] Q. M. Marashdeh, F. L. Teixeira, and L.-S. Fan, "Adaptive electrical capacitance volume tomography," *IEEE Sensors J.*, vol. 14, no. 4, pp. 1253–1259, Apr. 2014.

[29] J. Ye, H. Wang, and W. Yang, "Image reconstruction for electrical capacitance tomography based on sparse representation," *IEEE Trans. Instrum. Meas.*, vol. 64, no. 1, pp. 89–102, Jan. 2015.

[30] T. Dai and A. Adler, "Electrical impedance tomography reconstruction using l_1 norms for data and image terms," in *Proc. 30th Annu. Int. Conf. IEEE Eng. Med. Biol. Soc.*, Aug. 2008, pp. 2721–2724.

[31] R. Tibshirani, "Regression shrinkage and selection via the lasso," *J. Roy. Statist. Soc.*, vol. 58, no. 1, pp. 267–288, 1996.

[32] T. Hastie, R. Tibshirani, and J. Friedman, *The Elements of Statistical Learning: Data Mining, Inference, and Prediction*. New York, NY, USA: Springer Science+Business Media, 2009.

Peter Lindahl (S'08–M'15) received the Ph.D. degree in engineering from Montana State University, Bozeman, MT, USA, in 2013.

He is currently a Post-Doctoral Associate with the Research Laboratory of Electronics, Massachusetts Institute of Technology, Cambridge, MA, USA. His current research interests include nonintrusive sensing and instrumentation, smart-building technologies, energy efficiency, renewable energy generation, and energy policy.

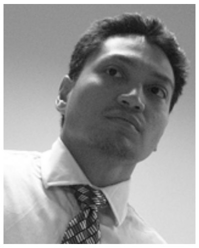

Al-Thaddeus Avestruz (S'04–M'15) received the Ph.D. degree in electrical engineering from the Massachusetts Institute of Technology, Cambridge, MA, USA, in 2015.

His research specialty is in the area of high performance power electronics, with complementary interests in circuits and systems for sensing, electromagnetic systems, feedback and controls, renewable energy, automotive, biomedical devices, and wireless power transfer technology. He is an Assistant Professor with the Department of Electrical and Computer Engineering, University of Michigan, Ann Arbor, MI, USA.

William Thompson received the B.S. and M.Eng. degrees in electrical engineering from the Massachusetts Institute of Technology, Cambridge, MA, USA, in 2010 and 2012, respectively.

He is currently with Apple Inc., Cupertino, CA, USA.

Elizabeth George received the B.S. and M.Eng. degrees in electrical engineering from the Massachusetts Institute of Technology, Cambridge, MA, USA, in 2012 and 2014, respectively.

She is currently with Silicon Labs, Austin, TX, USA.

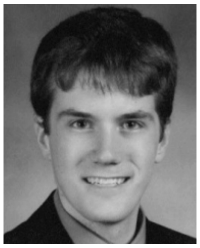

Brian R. Sennett received the B.S. and M.Eng. degrees in electrical engineering from the Massachusetts Institute of Technology, Cambridge, MA, USA, in 2013 and 2015, respectively.

He is currently with Bose Corporation, Framingham, MA, USA.

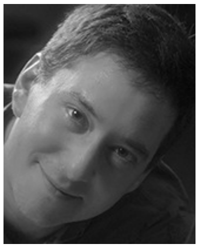

Steven B. Leeb (S'89–M'93–F'07) received the Ph.D. degree in electrical engineering and computer science from the Massachusetts Institute of Technology (MIT), Cambridge, MA, USA, in 1993.

He has been with the Department of Electrical Engineering and Computer Science, MIT, since 1994. He is currently a Professor with the Laboratory for Electromagnetic and Electronic Systems, MIT, where he is engaged in the design, analysis, development, and maintenance processes for all kinds of machinery and systems with electrical actuators, sensors, or power electronic drives.